Trapping and Counting Ballistic Nonequilibrium Electrons

Lars Freise [ORCID],[†] Thomas Gerster, David Reifert, Thomas Weimann, Klaus Pierz, Frank Hohls, and Niels Ubbelohde[*]

Physikalisch-Technische Bundesanstalt, Bundesallee 100, 38116 Braunschweig, Germany

We demonstrate the trapping of electrons propagating ballistically at far-above-equilibrium energies in GaAs/AlGaAs heterostructures in high magnetic field. We find low-loss transport along a gate-modified mesa edge in contrast to an effective decay of excess energy for the loop around a neighboring, mesa-confined node, enabling high-fidelity trapping. Measuring the full counting statistics via single-charge detection yields the trapping (and escape) probabilities of electrons scattered (and excited) within the node. Energetic and arrival-time distributions of captured electron wave packets are characterized by modulating tunnel barrier transmission.

The ability to prepare and subsequently detect discrete particles constitutes a crucial component for applications ranging from metrology over sensing to quantum information technologies, for example in utilizing single ions [1] or electrons [2] for quantum computation, or photons for quantum cryptography [3]. In electron quantum optics (EQO), the solid-state analog to quantum optics, the recent introduction of on-demand single-electron sources is advancing experiments that have previously been realized with continuous electron sources [4–9] by offering an inherent time control, for instance in mesoscopic capacitors [10–12], leviton injections [13], single-electron pumps (SEPs) [14–16], or the application of surface acoustic waves (SAWs) [17,18]. However, implementing a single-electron detector for an EQO experiment with ballistic electrons poses the challenge to detect ballistic electrons either on-the-fly or to trap them prior to detection. Combining single-particle detection with an on-demand single-particle source provides direct access to the full counting statistics, independent of the bosonic or fermionic nature of the observed particles, and ensures high signal fidelities even in circuits with simultaneous multiparticle injection. Additionally, multiple detectors can easily be combined and inherently record coincidence correlations.

Here, we present a single-electron circuit that traps ballistic electrons emitted from an SEP source at nonequilibrium energies of some 10 meV. Continuous-current measurements characterize low-loss electron propagation towards a node, where single-electron counting provides a measure of the high scattering probability enabling trapping. This technique resembles "sample and hold" circuits in analog electronics, where a voltage is sampled by charging a capacitor that retains the voltage for readout. The single-electron counterpart consists of four functional elements: an electron is emitted on-demand (source) and ballistically traverses a waveguide section (WG). At the circuit's output, the electron is then trapped inside a node by energy relaxation (capture) and read out (detect). This requires different propagation characteristics between waveguide (ideally lossless transport) and capture-node (ideally complete loss of excess energy) [Fig. 1(b)], which will be analyzed throughout this Letter. Following the denotation of detection efficiencies η to register a photon at the detector, which is one of the key parameters in quantum optics setups [19], separate coefficients η_{source}, η_{WG}, η_{capture}, and η_{detect} are assigned to the functional components, where $(1 - \eta_{\text{WG}})$ and η_{capture} express the scattering probabilities in the waveguide and on the node, respectively, and $\eta_{\text{circuit}} = \eta_{\text{source}} \eta_{\text{WG}} \eta_{\text{capture}} \eta_{\text{detect}}$.

The two circuit geometries investigated [samples A and B, Figs. 1(a) and S1 [20], respectively] have been realized [21] in the same GaAs/AlGaAs heterostructure with 97 nm nominal 2DEG depth, charge carrier density 1.9×10^{11} cm^{-2}, mobility 1.15×10^{6} cm^2 V^{-1} s^{-1}, and quantum life time 2.9 ps [22]. Components are formed by Cr/Au gates upon a shallow-etched channel. Measurements are carried out in a dry dilution refrigerator with base temperature below 50 mK and at 10 T perpendicular magnetic field ($\nu \approx 1$).

A nonadiabatic single-parameter single-electron pump [14,23,24] is used as an on-demand source of nonequilibrium electrons. It is confined by three gates (pump entrance and exit barriers G_{P1} and G_{P2}, side gate G_{P3}) and excited by a $f = 300$ MHz sinusoidal pulse on G_{P1}. The several-10-meV excess energy of the emitted electrons scales with G_{P2}'s barrier height [15,25] and separates
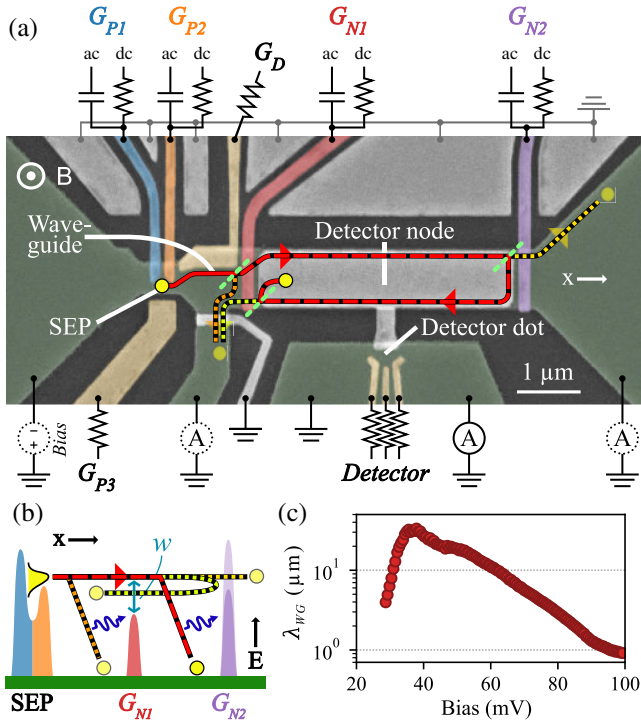
FIG. 1. (a) False color SEM micrograph of sample A with measurement setup (dotted: bias source and ammeters exclusively employed for precharacterization [20]). Active regions are colored [mesa "green," dc-only gates (yellow), dc-and-ac gates (different colors)]. Red, orange, and yellow lines sketch possible transport paths for an electron (yellow dot), potential barrier transmissions of an electron are indicated as green beam splitters. (b) Sketched energy diagram showing the different propagation paths. (c) Bias-dependent scattering length λ_{WG} (sample B, $V_{G_D} = 0$ mV).

transport from the Fermi sea. In continuous operation, this would correspond to a generated current $I = ef \approx 48$ pA with elementary charge e. SEPs have been reported in metrological applications with sub-ppm accuracy [26] and hence do not currently limit the circuit fidelity. Here, $\eta_{\mathrm{source}} \approx 0.999$ is estimated from the difference of measured continuous current to ef (not shown).

In perpendicular magnetic field, the injected electrons propagate along the sample edge with an imposed chirality, as in a ballistic waveguide. The confinement potential of this edge determines scattering cross sections and thereby the contributions of scattering mechanisms affecting propagating electrons. The electrons' injection energies substantially exceed those of systems in the integer quantum Hall effect $\nu = 2$ regime at excess energies $\ll 1$ meV, where relaxation mechanics have extensively been elaborated (e.g., [12,27–31] and references therein). In the waveguide section, the etch-defined edge potential is modulated by an edge-depletion gate G_D (here biased by $V_{G_D} = -350$ mV; stated voltages generally refer to signal's dc parts), introduced for suppression of electron-electron interactions [32] and shown to modulate and suppress longitudinal optical

(LO) phonon emission rates [32,33] by minimizing scattering cross sections and spatially separating transport from the mesa edge. Sample A is designed with a short waveguide length $l_{\mathrm{WG}} \approx 1.25$ μm to characterize scattering on the node unimpeded by residual losses in the waveguide. The survival probability P_S of an electron ballistically reaching the detector node, equivalent to η_{WG}, is obtained from the continuous current transmitted over the node entrance barrier G_{N1} (not shown) as $P_S = \eta_{\mathrm{WG}} \approx (0.997/\eta_{\mathrm{source}}) \approx 0.998$. A characteristic scattering length λ can be estimated in a simple, exponential model [33–35] from $P_S = \exp(-l/\lambda)$, yielding $\lambda_{\mathrm{WG}} \approx 0.5$ mm $\gg l_{\mathrm{WG}}$, which expresses low-loss ballistic transport.

Sample B (Fig. S1 [20]) integrates more components and an increased waveguide length of $l_{\mathrm{WG}} \approx 3$ μm to demonstrate the functionality in more complex circuitry (data is marked explicitly).

Hot-electron measurements (as in [20,35]) characterize the P_S of ballistic electrons as a function of injection bias, yielding an energy-dependence of λ_{WG} that is exemplarily depicted in Fig. 1(c) [36]: at small injection energies E, electron-electron interactions dominate λ_{WG} [35,37] by fully suppressing P_S (consistent with Ref. [35], which describes the effect of electron-hole excitation by the injected hot electrons via a phenomenological, length-dependent threshold energy E_{th}). Maximal λ_{WG} is attained above E_{th} (at few 10 mV bias), where the wave function overlap for electron-electron scattering is reduced and LO phonon emission not yet possible, before λ_{WG} deteriorates with further increasing E, in accordance with enhancing LO phonon emission [20,38,39]. Consequently, for EQO the injection energy of on-demand electrons should target the intermediate regime of optimal λ_{WG}. In the waveguide section, λ_{WG} is enhanced by modulating the edge potential via increasingly negative V_{G_D}, similar to observations in Ref. [33], however, it levels near $V_{G_D} \approx -300$ mV. Extracting the confinement potential to enable calculation of predicted LO phonon emission rates [32,33,38] is inhibited by geometric restrictions preventing the required time-of-flight measurements. However, comparing λ_{WG} to results in Ref. [33] indicates phonon emission rates similarly exceeding model predictions [40], substantiating the presence of additional processes, possibly indirect LO phonon emission involving supplemental longitudinal acoustic phonon emission [33,39].

Electrons that scattered while propagating through the waveguide are reflected by G_{N1} and sunk into an ohmic side contact. Propagation across the node in an etch-defined mesa-edge potential is investigated by recording η_{capture} of trapped electrons within a counting scheme, yielding a combined scattering probability of all mechanisms contributing to trapping. A distance of 4.2 μm between G_{N1} and node exit barrier G_{N2} creates a large node extent, forming an elongated quantum dot with lithographic circumference of 10.4 μm and typical charging energy of
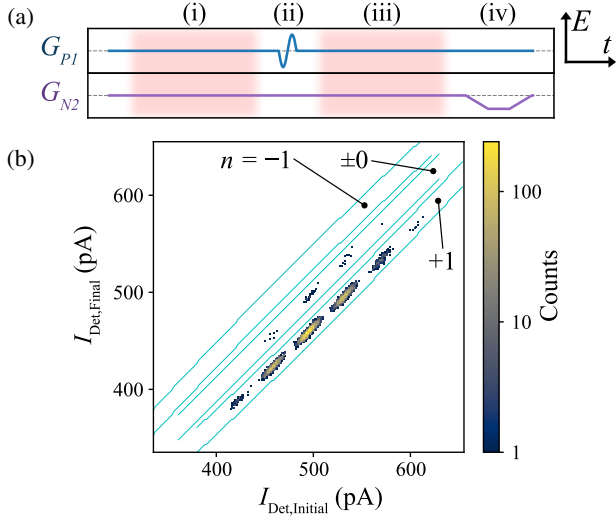
FIG. 2. (a) Sketched sequence of ac modulations built from four intervals [initial (i), final (iii) detector state readout (marked in red), (ii) electron transport, (iv) reset; not to scale] used for each measurement cycle. (b) Exemplary counting histogram [$V_{G_{N1}} = -334$ mV in Fig. 3(a)]. Measured detector signal is categorized into 200 bins and shown as final over initial detector state. Cyan lines enclose counts identifying a change by -1, 0, or $+1$ electrons.

few ten μeV. Assuming drift velocities of magnitude 5×10^4 m s^{-1} [32,33] would imply node transit times below 100 ps, distinctly exceeding reported temporal wave packet extents of few ten picoseconds [41–43].

The detector dot is formed by split gates against the edge of a separate mesa structure, an additional floating gate increases capacitive coupling to the node. Separation of the two mesas avoids the strong electrostatic screening and resulting reduction in detector resolution accompanying complete split-gate realizations [44]. The detector dot is operated in the Coulomb blockade regime to record charge changes on the node, with two readouts per repetition of the counting cycle, following the sequence depicted in Fig. 2(a): after completing the first readout [of the initial detector state, (i)], emission of an electron is triggered (ii), while after the second readout [final detector state, (iii)], the node state is reset (iv). The cycle repetition rate of 24 Hz is dominated by the charge-detection bandwidth of detector dot readout (62.5 to 83.3 Hz) and is limited by the coupling of an added electron onto the detector dot (which was observed to decrease with increasing node size and incomplete floating-gate coverage), the detector dot sensitivity and the required signal-to-noise ratio.

To estimate η_{capture} and η_{detect}, 10^5 cycles are recorded and the data binned into a 2D histogram, depicting final over initial detector state. Exemplary data can be seen in Fig. 2(b), where counts on the diagonal represent constant detector signals (i.e., node's charge state remains unchanged within a given cycle), while off-diagonal signatures reflect changes in the deposited charge. Multiple clusters emerge, clearly

separated in the x direction [corresponding to a varying node occupation in interval (i) due to the reset (iv)] and in the y direction [corresponding to electrons emitted on demand in interval (ii)]. Despite the large node size of > 4 μm^2, a peak separation of $\geq 5\sigma$ [20] is achieved. With $1 - \eta_{\text{detect}} \lesssim 10^{-6}$, identification errors do not limit η_{circuit}. The counts are summed to N_n [cyan lines in Fig. 2(b)] and lead to the full counting statistics $P_n = (N_n / \sum_i N_i)$ of a change in the node's charge by n electrons. The high probability $P_1 \approx 0.996$ indicates efficient scattering of electrons in this segment and is equivalent to the achieved maximal circuit fidelity, $\eta_{\text{circuit}} \approx 0.996$, revealing the near-unity $\eta_{\text{capture}} = (\eta_{\text{circuit}} / \eta_{\text{source}} \eta_{\text{WG}} \eta_{\text{detect}}) \approx 0.999$ that is similarly reproduced in sample B (cf. [20]). The achievable fidelity of these circuits is largely limited by transport properties of the waveguide and compares well to fidelities of (nonballistic) electron transport inside SAW-induced moving quantum dots [17,45].

For the trapping of on-demand electron wave packets, it is particularly important to also consider the intrinsic energy-time correlation of the wave packets emitted by SEPs [46,47]. Within our trap-and-detect scheme, these wave packet characteristics are in the following accessed by utilizing the energy-dependent transmission of the node-defining barriers [15,16,32,41,43,47]. The resulting tomographic projections of the wave packet furthermore provide the basis for the synchronization of energetic, temporal, and spatial wave packet overlaps required for interferences of electron wave packets in nonequilibrium EQO experiments.

Figure 3(a) demonstrates the progressive blocking of lower-energy electrons with increasing barrier height of G_{N1}, depicting the wave packet's energy distribution, with an asymmetry (cf. inset) caused by non-Gaussian emission characteristics of the SEP [46,47]. A relative energy-scale can be derived [20] and is displayed on the top axis of Fig. 3(a) (zero set for maximum electron energy arriving at G_{N1}). The energetic width of the distribution is evaluated as the transition's full width half maximum (FWHM) in $\partial P_n / \partial V_{G_{N1}}$ to $\delta E \approx 4$ meV and agrees well with other experiments [15,41,43]. This provides an upper bound to the energetic width of the wave packet [41] that is fundamentally limited by convolution with the barrier characteristics, the relative contribution of which is difficult to estimate even in a recent tomography scheme [47].

The SEP's emission energy E_0 considered so far within Fig. 3(a) lies in the maximal-λ_{WG} region, close to the gradual onset of LO phonon emission [20]. However, the emission energies of SEPs can span a large range, exceeding $E > 100$ meV [15,25]. Trapping at an increased emission energy E_1 is shown in Fig. 3(b) ($\Delta E_1 = E_1 - E_0 \approx 20$ meV [20], compare positions of both transitions in Fig. 3; energy increase by synchronized excitation of G_{P1} and G_{P2}) and exhibits consistently high $\eta_{\text{capture}}^{E_1} \approx \eta_{\text{capture}}^{E_0}$ despite the increased emission energy, as apparent from
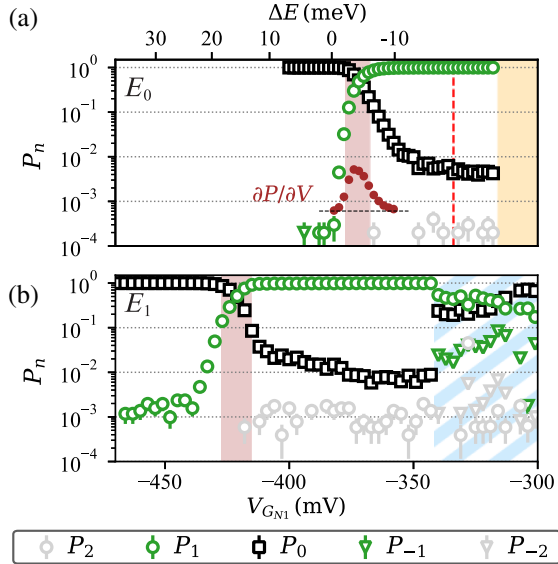
FIG. 3. Energy-dependent probabilities for detection of single electron wave packets depending on node entrance barrier heights for two electron emission energies E_0 (a) and $E_1 = E_0 + 20$ meV (b) plotted on identical scales (G_{N2} raised above emission energies). Barrier height increases to the left, transitions $P_1 \approx 1 \to P_1 \approx 0$ depict energy distributions of wave packets [48]. FWHMs are highlighted in dark red, (a) with inset of derivative $\partial P_1 / \partial V_{G_{N1}}$. Error bars represent statistical errors. Orange background and blue stripes mark regions inaccessible to detector readout (no clear, consistent charge state observable, hinting at nonlinear transmission properties of G_{N1}) and of missing electrons, respectively. Red line indicates the value taken for Fig. 4(a). $P_2 > 0$ due to nonideal SEP quantization.
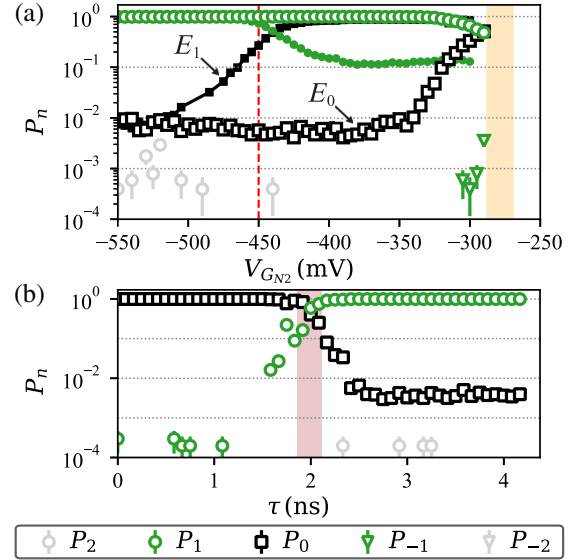

FIG. 4. (a) Energy-resolved capturing for G_{N2} probes scattering while traversing the node. Data shown at E_0 ($V_{G_{N1}}^{E_0} = -334$ mV) and E_1 (small markers; for clarity only P_0 and P_1 shown, $V_{G_{N1}}^{E_1} = -370$ mV). Opposed to Fig. 3, transmission over G_{N2} results in $n = 0$. Red line marks value taken for Fig. 3(a). (b) Time-resolved capturing at E_0 by raising G_{N1} at time delay τ relative to pump excitation (methods in [20]).

$\eta_{\text{circuit}}^{E_1} \approx 0.992$. The energetic width $\delta E^{E_1} \approx 5$ meV is also close to the lower-energy value. A larger energy increase by $\Delta E_2 \approx 50$ meV ($E_2 = E_0 + \Delta E_2$, data in [20]) yields $\delta E^{E_2} \approx 9.5$ meV and reduced $\eta_{\text{circuit}}^{E_2} \approx 0.90$, which however is mainly due to deteriorating quantization of the source, $\eta_{\text{source}}^{E_2}$. There is no discernible indication for a decrease in η_{capture} over the inspected 50 meV emission-energy range.

In the energy-resolved measurements at increased emission energies, additional signatures appear in the limit of small node entrance barrier heights [blue stripes in Fig. 3(b), [49]], where P_1 drops for decreasing barrier heights, while P_0 increases and in some cycles the charge on the node is reduced, $P_{-1} > P_{-2} > 0$. The appearing $P_{-1}, P_{-2} > 0$ cannot be plausibly explained as a modulation of source, waveguide, or detector functionality and is directly related to electrons emitted from the SEP [50]. We interpret $P_{-1}, P_{-2} > 0$ as a process of energy redistribution from relaxation of the hot electron, similar to observations in Ref. [51], enabling thereby excited electrons to escape the node. At E_2, this region extends towards stronger negative $V_{G_{N1}}$, in accordance with the increased energy available for redistribution upon scattering. Including P_{-2},

four nonzero elements of the full counting statistics are recorded within the low-barrier limit of Fig. 3(b), highlighting the benefit of the single-electron resolution.

The wave packet's energy distributions at G_{N2} are depicted in Fig. 4(a), probing scattering while traversing the node. At E_0, no survival probability of electrons ballistically traversing the node is resolved [$P_S^{E_0} \approx 0$, visible from (incomplete) wave packet mapping only at vanishing barrier heights]. Thus, merely by taking into account scattered electrons maintaining sufficient energy to pass small G_{N2}, $P_{\text{Max.transmission}} \approx 0.52$ can be used to estimate an upper limit for $\lambda_{\text{Node}}^{E_0} \ll 6.5$ μm. This represents, in contrast to propagation in the gate-modified potential of the wave-guide section, a change of approximately two orders of magnitude for transport through the etch-defined edge potential and for E_0 close to the energetic regime of strong electron-electron scattering (cf. [20]).

At the increased emission energy E_1, however, a substantial ballistic survival probability $P_S^{E_1} \approx 0.88$ is evident from the clear transition detected at elevated barrier G_{N2} [also Fig. 4(a)], corresponding to $\lambda_{\text{Node}}^{E_1} \approx 34$ μm. $\lambda_{\text{Node}}^{E_1} > l_{\text{Node circumference}}$ would suggest a pronounced fraction of electrons being able to escape the node after traversing its circumference in a full loop. This is however contradicted by the miniscule escape probabilities seen in the low-barrier limits of Fig. 3, which indicate an even further reduced scattering length with near-unity η_{capture}s. We conclude that more mechanisms beyond the changing edge potential are

contributing to these high trapping fidelities, for example backactions of the active charge detector [52]. The combined scattering probability, however, methodically cannot identify individual scattering mechanisms. Furthermore, additional modifications of scattering may result from the node being isolated, e.g., by loop excitations ($E_{\text{Loop excitation}} \ll E_0$), as for example observed in Ref. [53]. Manipulating the node's electrochemical potential or, via in-plane gating, its edge-potential profile did not measurably enhance η_{capture}. Ultimately, defining a narrow, energy-selective "capture window" [labeled w in Fig. 1(b)] would allow for detecting energetically sharp, incident electron wave packets even after minor energy losses.

The wave packet's arrival-time distribution at G_{N1} is pictured in Fig. 4(b) as a function of the time delay τ at which G_{N1} is raised to block the incident wave packets from entering the node (cf. [20]). Its relatively wide FWHM $\delta t \approx$ 250 ps is an upper bound to the temporal width of the electron wave packet [20], limited by barrier characteristics but consistent with the dependence on the SEP's operating point [15,46,47]. Despite δt being of the same order of magnitude as the estimated transit time around the node, the distinct trapping capability persists due to the high scattering probability on the node preventing electrons from exiting after fully traversing its circumference. This technique of time-resolved detection also constitutes the minimal module for a proposed single-shot voltage sampling [43].

In conclusion, strongly differing scattering probabilities were measured in neighboring segments of a single-electron circuit, allowing capturing and detection of single electrons after ballistic propagation, resolving the full counting statistics and estimating wave packet characteristics. The resolution of these can prospectively be enhanced by manipulating SEP emission characteristics and applying tomographic schemes [47] or optimizing barrier characteristics [54]. The demonstrated robustness of detection to shifting injection energies is especially important for future collision and interferometry experiments requiring an energetic overlap between wave packets emitted from independent nonequilibrium sources.

[*]Corresponding author.
niels.ubbelohde@ptb.de
[†]lars.freise@ptb.de

[1] J. I. Cirac and P. Zoller, Phys. Rev. Lett. **74**, 4091 (1995).

[2] A. Imamoglu, D. D. Awschalom, G. Burkard, D. P. DiVincenzo, D. Loss, M. Sherwin, and A. Small, Phys. Rev. Lett. **83**, 4204 (1999).

[3] N. Gisin, G. Ribordy, W. Tittel, and H. Zbinden, Rev. Mod. Phys. **74**, 145 (2002).

[4] M. Henny, S. Oberholzer, C. Strunk, T. Heinzel, K. Ensslin, M. Holland, and C. Schönenberger, Science **284**, 296 (1999).

[5] W. D. Oliver, J. Kim, R. C. Liu, and Y. Yamamoto, Science **284**, 299 (1999).

[6] R. C. Liu, B. Odom, Y. Yamamoto, and S. Tarucha, Nature (London) **391**, 263 (1998).

[7] Y. Ji, Y. Chung, D. Sprinzak, M. Heiblum, D. Mahalu, and H. Shtrikman, Nature (London) **422**, 415 (2003).

[8] I. Neder, N. Ofek, Y. Chung, M. Heiblum, D. Mahalu, and V. Umansky, Nature (London) **448**, 333 (2007).

[9] C. Bäuerle, D. C. Glattli, T. Meunier, F. Portier, P. Roche, P. Roulleau, S. Takada, and X. Waintal, Rep. Prog. Phys. **81**, 056503 (2018).

[10] G. Fève, A. Mahé, J.-M. Berroir, T. Kontos, B. Plaçais, D. C. Glattli, A. Cavanna, B. Etienne, and Y. Jin, Science **316**, 1169 (2007).

[11] E. Bocquillon, F. D. Parmentier, C. Grenier, J.-M. Berroir, P. Degiovanni, D. C. Glattli, B. Plaçais, A. Cavanna, Y. Jin, and G. Fève, Phys. Rev. Lett. **108**, 196803 (2012).

[12] E. Bocquillon, V. Freulon, J.-M. Berroir, P. Degiovanni, B. Plaçais, A. Cavanna, Y. Jin, and G. Fève, Science **339**, 1054 (2013).

[13] J. Dubois, T. Jullien, F. Portier, P. Roche, A. Cavanna, Y. Jin, W. Wegscheider, P. Roulleau, and D. C. Glattli, Nature (London) **502**, 659 (2013).

[14] M. Blumenthal, B. Kaestner, L. Li, S. Giblin, T. Janssen, M. Pepper, D. Anderson, G. Jones, and D. Ritchie, Nat. Phys. **3**, 343 (2007).

[15] J. D. Fletcher, P. See, H. Howe, M. Pepper, S. P. Giblin, J. P. Griffiths, G. A. C. Jones, I. Farrer, D. A. Ritchie, T. J. B. M. Janssen, and M. Kataoka, Phys. Rev. Lett. **111**, 216807 (2013).

[16] N. Ubbelohde, F. Hohls, V. Kashcheyevs, T. Wagner, L. Fricke, B. Kästner, K. Pierz, H. W. Schumacher, and R. J. Haug, Nat. Nanotechnol. **10**, 46 (2015).

[17] S. Hermelin, S. Takada, M. Yamamoto, S. Tarucha, A. D. Wieck, L. Saminadayar, C. Bäuerle, and T. Meunier, Nature (London) **477**, 435 (2011).

[18] R. P. G. McNeil, M. Kataoka, C. J. B. Ford, C. H. W. Barnes, D. Anderson, G. A. C. Jones, I. Farrer, and D. A. Ritchie, Nature (London) **477**, 439 (2011).

[19] R. H. Hadfield, Nat. Photonics **3**, 696 (2009).

[20] See the Supplemental Material at http://link.aps.org/supplemental/10.1103/PhysRevLett.124.127701 for additional information on sample *B*, sample operation, and characterization.

[21] T. Gerster, A. Mueller, L. Freise, D. Reifert, D. Maradan, P. Hinze, T. Weimann, H. Marx, K. Pierz, H. W. Schumacher, F. Hohls, and N. Ubbelohde, Metrologia **56**, 014002 (2019).

[22] P. T. Coleridge, P. Zawadzki, and A. S. Sachrajda, Phys. Rev. B **49**, 10798 (1994).

[23] B. Kaestner, V. Kashcheyevs, S. Amakawa, M. D. Blumenthal, L. Li, T. J. B. M. Janssen, G. Hein, K. Pierz, T. Weimann, U. Siegner, and H. W. Schumacher, Phys. Rev. B **77**, 153301 (2008).

[24] N. Maire, F. Hohls, B. Kaestner, K. Pierz, H. W. Schumacher, and R. J. Haug, Appl. Phys. Lett. **92**, 082112 (2008).

[25] C. Leicht, P. Mirovsky, B. Kaestner, F. Hohls, V. Kashcheyevs, E. V. Kurganova, U. Zeitler, T. Weimann, K. Pierz, and H. W. Schumacher, Semicond. Sci. Technol. **26**, 055010 (2011).

[26] F. Stein, D. Drung, L. Fricke, H. Scherer, F. Hohls, C. Leicht, M. Götz, C. Krause, R. Behr, E. Pesel, K. Pierz, U. Siegner, F. J. Ahlers, and H. W. Schumacher, Appl. Phys. Lett. **107**, 103501 (2015).

[27] S. Tewari, P. Roulleau, C. Grenier, F. Portier, A. Cavanna, U. Gennser, D. Mailly, and P. Roche, Phys. Rev. B **93**, 035420 (2016).

[28] S. E. Nigg and A. M. Lunde, Phys. Rev. B **94**, 041407(R) (2016).

[29] E. Bocquillon, V. Freulon, F. D. Parmentier, J.-M. Berroir, B. Plaçais, C. Wahl, J. Rech, T. Jonckheere, T. Martin, C. Grenier, D. Ferraro, P. Degiovanni, and G. Fève, Ann. Phys. (N.Y.) **526**, 1 (2014).

[30] T. Krähenmann, S. G. Fischer, M. Röösli, T. Ihn, C. Reichl, W. Wegscheider, K. Ensslin, Y. Gefen, and Y. Meir, Nat. Commun. **10**, 3915 (2019).

[31] R. H. Rodriguez, F. D. Parmentier, P. Roulleau, U. Gennser, A. Cavanna, F. Portier, D. Mailly, and P. Roche, arXiv: 1903.05919.

[32] M. Kataoka, N. Johnson, C. Emary, P. See, J. P. Griffiths, G. A. C. Jones, I. Farrer, D. A. Ritchie, M. Pepper, and T. J. B. M. Janssen, Phys. Rev. Lett. **116**, 126803 (2016).

[33] N. Johnson, C. Emary, S. Ryu, H.-S. Sim, P. See, J. D. Fletcher, J. P. Griffiths, G. A. C. Jones, I. Farrer, D. A. Ritchie, M. Pepper, T. J. B. M. Janssen, and M. Kataoka, Phys. Rev. Lett. **121**, 137703 (2018).

[34] A. Palevski, M. Heiblum, C. P. Umbach, C. M. Knoedler, A. N. Broers, and R. H. Koch, Phys. Rev. Lett. **62**, 1776 (1989).

[35] T. Ota, S. Akiyama, M. Hashisaka, K. Muraki, and T. Fujisawa, Phys. Rev. B **99**, 085310 (2019).

[36] The different geometry of the waveguide section in sample B yields lower values of λ_{WG} compared to sample A.

[37] D. Taubert, C. Tomaras, G. J. Schinner, H. P. Tranitz, W. Wegscheider, S. Kehrein, and S. Ludwig, Phys. Rev. B **83**, 235404 (2011).

[38] C. Emary, A. Dyson, S. Ryu, H.-S. Sim, and M. Kataoka, Phys. Rev. B **93**, 035436 (2016).

[39] C. Emary, L. A. Clark, M. Kataoka, and N. Johnson, Phys. Rev. B **99**, 045306 (2019).

[40] Comparison bases on similar experimental conditions, i.e., matching magnitude of electron velocities, here inferred from magnetic-field dependence of λ_{WG} [35].

[41] J. Waldie, P. See, V. Kashcheyevs, J. P. Griffiths, I. Farrer, G. A. C. Jones, D. A. Ritchie, T. J. B. M. Janssen, and M. Kataoka, Phys. Rev. B **92**, 125305 (2015).

[42] M. Kataoka, J. D. Fletcher, and N. Johnson, Phys. Status Solidi B **254**, 1600547 (2017).

[43] N. Johnson, J. D. Fletcher, D. A. Humphreys, P. See, J. P. Griffiths, G. A. C. Jones, I. Farrer, D. A. Ritchie, M. Pepper, T. J. B. M. Jannsen, and M. Kataoka, Appl. Phys. Lett. **110**, 102105 (2017).

[44] C. Rössler, B. Küng, S. Dröscher, T. Choi, T. Ihn, K. Ensslin, and M. Beck, Appl. Phys. Lett. **97**, 152109 (2010).

[45] S. Takada, H. Edlbauer, H. V. Lepage, J. Wang, P.-A. Mortemousque, G. Georgiou, C. H. W. Barnes, C. J. B. Ford, M. Yuan, P. V. Santos, X. Waintal, A. Ludwig, A. D. Wieck, M. Urdampilleta, T. Meunier, and C. Bäuerle, Nat. Commun. **10**, 4557 (2019).

[46] V. Kashcheyevs and P. Samuelsson, Phys. Rev. B **95**, 245424 (2017).

[47] J. D. Fletcher, N. Johnson, E. Locane, P. See, J. P. Griffiths, I. Farrer, D. A. Ritchie, P. W. Brouwer, V. Kashcheyevs, and M. Kataoka, Nat. Commun. **10**, 5298 (2019).

[48] Leftmost "P_1" markers in (a) represent insufficient statistics (not nonzero leveling), P_1 leveling at 10^{-3} in (b) might result from complex rf excitation occasionally producing even-higher-energy electrons.

[49] Histogram evaluation in this region is complicated due to electron tunneling *simultaneously* to data acquisition. This significantly reduces the fidelity but does not challenge the existence of the feature itself.

[50] These events are not a parasitic effect, e.g., by coupling of the SEP excitation onto G_{N1}. $P_{-2} = P_{-1} = 0$ is restored if electron emission is suppressed (by raising G_{P2} or by turning off one or both SEP excitations).

[51] D. Taubert, G. J. Schinner, H. P. Tranitz, W. Wegscheider, C. Tomaras, S. Kehrein, and S. Ludwig, Phys. Rev. B **82**, 161416(R) (2010).

[52] D. Harbusch, D. Taubert, H. P. Tranitz, W. Wegscheider, and S. Ludwig, Phys. Rev. Lett. **104**, 196801 (2010).

[53] C. Altimiras, H. le Sueur, U. Gennser, A. Cavanna, D. Mailly, and F. Pierre, Phys. Rev. Lett. **105**, 226804 (2010).

[54] E. Locane, P. W. Brouwer, and V. Kashcheyevs, New J. Phys. **21**, 093042 (2019).